



Support effects of NiW catalysts for highly selective sulfur removal from light hydrocarbons



J.N. Díaz de León ^{a,*}, L.A. Zavala-Sánchez ^a, V.A. Suárez-Toriello ^b, G. Alonso-Núñez ^a, T.A. Zepeda ^a, R.I. Yocupicio ^a, J.A. de los Reyes ^b, S. Fuentes ^a

^a Universidad Nacional Autónoma de México, Centro de Nanociencias y Nanotecnología, Km. 107 carretera Tijuana-Ensenada, C.P. 22800, Ensenada, Baja California, Mexico

^b Departamento de Ciencias Básicas e Ingeniería, UAM-Iztapalapa, San Rafael Atlixco 186, Col. Vicentina, Iztapalapa, D.F. 09340, Mexico

ARTICLE INFO

Article history:

Received 16 February 2017

Received in revised form 27 April 2017

Accepted 3 May 2017

Available online 4 May 2017

Keywords:

Hydrotreatment

Hydrodesulfurization

Support effect

Supported catalysts

Sulfur removal

NiWS

ABSTRACT

The intrinsic support effect was explored in the preparation of NiW hydrodesulfurization catalysts through building correlations of catalytic performance to extensive surface characterization results. We found that the catalytic activity on the hydrodesulfurization of 3-methyl-thiophene correlates well with the normalized intensities data of NO adsorbed on Ni active sites. Also, a correlation between the catalytic activity and the number of tungsten edge atoms in the WS₂ slabs was observed. The characterization of the NiW catalysts revealed that is possible to modulate the metal-support interaction by substituting the carrier. This specific interaction with each support derived into particular morphological parameters for the sulfide active phase. Optimal values for the slab length and the stacking of the WS₂ slabs were proposed.

© 2017 Elsevier B.V. All rights reserved.

1. Introduction

More stringent environmental regulations have been implemented to reduce the sulfur content of gasoline and diesel fuels to ever lower levels. In Europe and the USA, sulfur content limits of about 10–50 ppm in gasoline and diesel are thus required. Furthermore, these sulfur levels are expected to be lowered to 10 ppm or less, and the “zero sulfur” emissions are targeted shortly [1]. Moreover, the sulfur must be removed selectively from aromatic thiophene and its derivatives from gasoline, keeping at a minimum the olefins hydrogenation (HYD) [2]. It has to be considered that the fluid catalytic cracking (FCC) naphtha stream at the refinery is usually used for the production of clean gasoline. This stream contains undesired organic sulfur compounds and is rich in olefins. Therefore, a careful removal of the sulfur-containing compounds without olefin saturation is highly needed. In that sense, we recently reported enhanced catalytic activity and excellent selectivity with the use of supported NiW catalysts. These catalysts supported on Al₂O₃-Ga₂O₃ binary mixed oxides showed that the 3-methyl thiophene (3MT) hydrodesulfurization (HDS) reaction

preferentially occurred by the direct desulfurization pathway [3]. Likewise, a linear increment of the hydrogenation pathway was observed with the increase of Ga₂O₃ wt.% in the support composition. Therefore, we confirmed that the catalytic activity of HDS catalysts might increase by changing the nature of the support [4]. Additionally, clear differences in the formation of the sulfide active phases, morphology, dispersion and sulfiding capacity have been discussed in a wide number of reports as a function of the chosen support [5–9]. Some carriers may impart four to five folds higher activities in typical CoMo and NiMo HDS catalysts as compared with Al₂O₃. However, the vast majority of research on HDS materials have been done concerning the CoMo and NiMo systems, and that acquired knowledge has been extended to the NiW system by similarity. Furthermore, direct information for the NiW system is scarcely found despite the fact that NiW catalysts have shown different sulfidation and catalytic activity [10]. Also, some early studies indicate that the NiW base catalysts could perform high HDS while promoting olefin skeletal isomerization [11,12]. This property of the NiW base catalysts helps to increase the octane number again and compensate the olefin saturation.

In the light of previous findings, we have focused the present work on elucidating the support effects for the NiW based catalysts. Hence, NiW catalysts supported on Al₂O₃, TiO₂, ZrO₂, and SiO₂ as well as on Al₂O₃-TiO₂ and ZrO₂-TiO₂ mixed oxides were

* Corresponding author.

E-mail address: noejd@cny.unam.mx (J.N. Díaz de León).

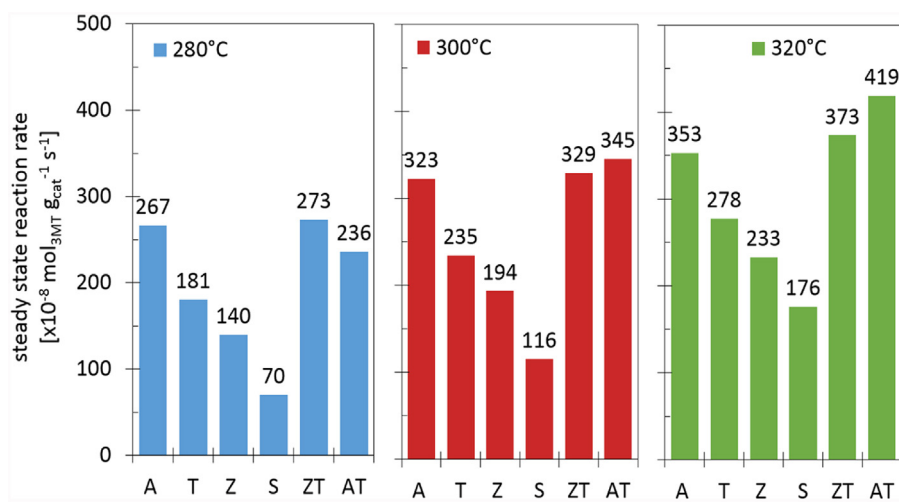


Fig. 1. Steady state catalytic activities for NiW-x catalysts in the HDS of 3MT.

prepared and widely characterized. The physicochemical properties of the supports and catalysts were explored by a variety of techniques (N_2 physisorption, XRD, TPD-NH₃, FT-IR of NO adsorbed and HRTEM). All materials were tested on atmospheric 3-methylthiophene (3MT) HDS as olefin model molecule.

2. Experimental section

2.1. Supports preparation

Pure γ -Al₂O₃ (A), SiO₂ (S), TiO₂ (T), ZrO₂ (Z) and mixed Al₂O₃-TiO₂ (AT) and ZrO₂-TiO₂ (ZT) supports were synthesized by sol-gel method. The sol-gel method was as follows: 10 mL of metal oxide precursor (*full list of precursors are given as Supplementary information A1*) were dissolved in 166 mL of 2-propanol (Aldrich 98%) under continuous stirring for 2 h at 0 °C. Subsequently, the hydrolysis solution (a mixture of 11.5 mL H₂O and 0.57 mL HNO₃ 70%) was added dropwise to the previous solution. The sol was left at 0 °C for 24 h to form the gel and then it was put into a crystallizer at 70 °C for 48 h to eliminate the solvent. The obtained solids were calcined at 500 °C for 4 h with a heating rate of 1 °C min⁻¹. The AT mixed oxide was prepared with an atomic ratio (Al/Ti) = 2 [13], for the ZT material the atomic ratio (Zr/Ti) was fixed at 1 [14]. In the case of the SiO₂ (S) material, 1 g of P123 (MW 5800, Aldrich) was dispersed in an HCl solution (0.1 g, 2 M) and H₂O (0.9 g) in EtOH (10 g). After 2 h of stirring, TEOS (2.08 g, 10 mMol) was added. The solution was aged for 24 h and then dried at 120 °C. Finally, the white solid was calcined at 500 °C for 4 h with a heating rate of 1 °C min⁻¹.

2.2. Catalysts preparation

In a typical preparation of NiW/(x) catalyst (where x is any of the supports), a solution of (NH₄)₆W₁₂O₃₉·xH₂O (AMT, Aldrich Chemical, 99.99%) was first impregnated on the support. Later, it was left for maceration for 12 h and then dried under an air stream at 125 °C for 12 h, with a heating rate of 3 °C min⁻¹. Finally, Ni was impregnated under the same conditions, and the green final solid was dried in the same terms. The concentration of AMT solution was selected to obtain 2.8 W atoms nm⁻² (pH ≈ 3.7) while nickel was adjusted to define a nominal atomic ratio $r = (Ni/(Ni + W))$ equal to 0.41 (pH ≈ 4). After calcination at 450 °C, all materials were sieved between 80 and 100 mesh (0.15–0.18 mm). Similar impregnation procedures were used to compare materials with very different surface areas [15,16].

2.3. Characterization methods

2.3.1. N_2 adsorption–desorption isotherms

The textural properties of the materials were determined by N_2 adsorption–desorption isotherms at -196 °C on a TriStar II 2020 Micromeritics equipment. Before the experiments, the materials were degassed at 125 °C in vacuum for 5 h. The volume of the adsorbed N_2 was normalized to the standard temperature and pressure. Specific surface areas (S_{BET}) were calculated by the Brunauer–Emmet–Teller (BET) equation, considering the range of relative pressures $0.1 < P/P_0 < 0.3$. The average pore diameter (P_d) was calculated by applying the Barret–Joyner–Halenda method (BJH) to the adsorption branches of the N_2 isotherms. The total pore volume (P_v) was obtained from the saturation point ($P/P_0 \sim 0.99$).

2.3.2. X-ray diffraction

X-ray diffraction (XRD) measurements of the samples were performed in a Philips spectrometer model X'pert using the CuK_α1 radiation (40 kV, 30 mA) with a wavelength of 0.154 nm.

2.3.3. Temperature programmed desorption of ammonia (TPD-NH₃)

The acidities for the oxide precursors were determined by TPD-NH₃ measurements carried out with an AMI 90 TPR/TPD instrument with a thermal conductivity detector (TCD) and interfaced to a data station. The catalysts (50 mg) were placed inside a 4 mm ID U-shaped quartz tube. Before ammonia adsorption, the catalysts were heated at a rate of 10 °C min⁻¹ to a final temperature of 200 °C and kept for 0.5 h at this temperature under a He flow to remove water and other contaminants. Then the samples were cooled down to 100 °C, and the surface was ammonia-saturated on a stream of 50 mL min⁻¹ of 5 mol% ammonia in He during 1 h. After catalysts equilibration in He flow at 100 °C for 15 min, ammonia was desorbed using a linear heating rate of 10 °C min⁻¹ to 900 °C.

2.3.4. Fourier transform infrared spectroscopy (FT-IR) of adsorbed NO on the sulfided catalysts

Fourier transform infrared spectroscopy (FT-IR) of adsorbed NO on the sulfided catalysts was recorded on an Agilent 660 FTIR spectrophotometer at a resolution of 4 cm⁻¹ with a specially designed Praying Mantis diffuse reflection attachment and low-temperature cell (Harrick) for *in situ* measurements. The samples were outgassed at 350 °C for 2 h and cooled down to 25 °C before contact with ca. 20 mbar of nitrogen monoxide for 5 min, after which the spectrum was recorded. Then the samples were degassed under

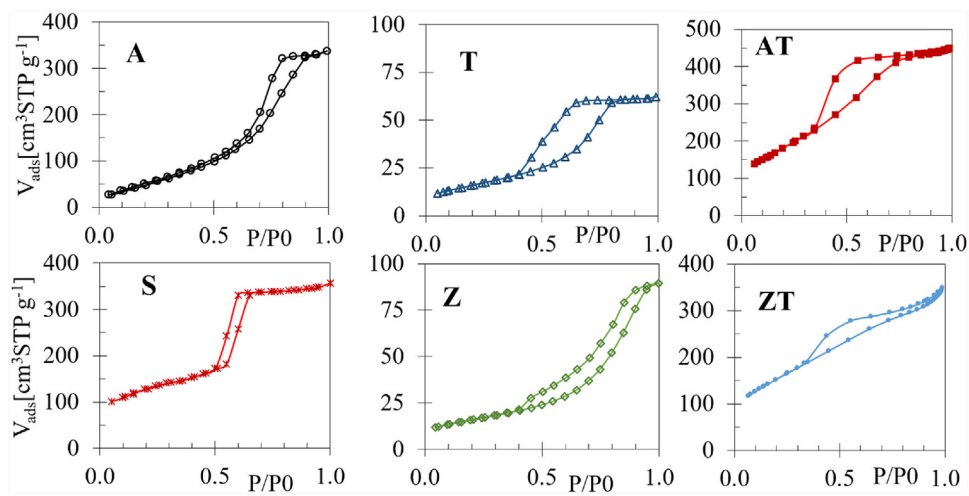


Fig. 2. Nitrogen adsorption-desorption isotherms for samples a) A, T, Z, S, ZT and AT calcined at 500 °C.

Table 1

Selectivity and DDS product yields at 280 °C for the NiW catalysts at steady state conversions.

NiW Catalysts	Selectivity at 280 °C		DDS Product yields%		
	%HYD	%DDS	Isoprene	1 st HYD (C ₅ -Olefins)	2 nd HYD iC ₅
A	0.3	99.7	21.4	78.4	0.2
T	1.4	98.6	24.5	74.4	1.1
Z	1.3	98.7	24.4	75.1	0.5
S	2.1	97.9	21.6	77.1	1.3
ZT	4.2	95.8	25.2	72.1	2.7
AT	2.4	97.6	28.1	69.7	2.2

10⁻⁵ mbar at 350 °C for 2 h to achieve total desorption of the NO molecules, and the spectrum of the catalyst was recorded. The IR spectrum of the adsorbed NO was obtained by subtracting the spectrum of the corresponding catalyst degassed under vacuum at 350 °C.

2.3.5. High-resolution transmission electron microscopy (HRTEM)

HRTEM micrographs were collected on a JEOL-2010F instrument. Samples were suspended in *n*-heptane as a solvent to be deposited on lacey carbon (440 Mesh) Cu grid holders.

2.4. Catalytic activity measurements

The catalysts were activated by in-situ sulfidation in the reactor with a stream of the sulfidation mixture (H₂/H₂S 15% v/v H₂S) with a flow of 40 mL min⁻¹ and then increasing the temperature up to 400 °C in ca. 2.5 h. The sulfidation continued under these conditions for 4 h. Afterward, the sample was cooled down to room temperature, changing the sulfidation flow to the reaction mixture when the temperature had reached 150 °C. The 3-methyl thiophene (3MT) HDS reaction was carried out in a biphasic continuous microflow reactor operating under atmospheric pressure. The saturator with 3MT (Aldrich Chemical 99.9%) was established to 19 °C, and then 40–100 cm³ min⁻¹ of H₂ flow were sent through downstream. The flow was controlled at an adequate value to avoid high conversions (~70 cm³ min⁻¹). The reaction was tested at three different temperatures (280 °C, 300 °C and 320 °C) using 50–100 mg of pre-activated catalyst. The spent sulfided catalysts were recovered and suspended in *n*-heptane to carry out the HRTEM analysis.

3. Results

3.1. 3-Methyl-thiophene transformation

The 3-methyl thiophene (3MT) steady state catalytic activities and selectivities for the supported NiW catalysts are shown in Fig. 1 and Table 1, respectively. Catalytic activities at different temperatures indicate that the largest intrinsic activity was displayed by the NiW/AT catalysts at 300 °C and 320 °C. Meanwhile, the activities of NiW/ZT and NiW/A catalysts were comparable throughout the range of tested temperatures (280–320 °C). Clearly the NiW/ZT sulfidized material showed the highest catalytic activity at the lowest temperature (280 °C). Notably, the NiW/A catalyst also resulted more active than the NiW/AT catalyst at low temperature. According to Breyssse et al. [7] the NiW catalysts supported on alumina, titania and zirconia exhibited the following behavior in the thiophene HDS reaction: NiW/A > NiW/Z > NiW/T. Furthermore, the catalytic activity of the NiW/T catalyst in the thiophene HDS reaction was reported by some authors higher than that of the NiW/A [17]. Although we expected a similar behavior, our experimental results revealed that for 3MT model molecule, the catalyst supported on alumina displayed higher activity than NiW/T and NiW/Z. It is noteworthy that the NiW/T resulted in average 19% greater than NiW/Z material in all the range of temperatures. As expected, the NiW/S catalytic system displayed the lowest catalytic activity among the series across the range of temperatures. Several siliceous materials have been tested as supports for HDS catalysts with promising results. i.e. well-ordered mesoporous molecular sieves as the HMS [18] or the SBA [19,20]. Nevertheless, high activity was obtained only when the siliceous materials were doped with other metals such as Al or Ti. The general catalytic results pointed to a trend as follows: NiW/A > NiW/T > NiW/Z > NiW/S, and noticeably NiW/AT > NiW/ZT > NiW/A.

Table 2

Textural properties for all samples calcined at 500 °C.

Sample	S_{BET} [$\text{m}^2 \text{ g}^{-1}$]	P_v [$\text{cm}^3 \text{ g}^{-1}$]	P_d Å
A	320	0.97	98
T	55	0.11	40
Z	78	0.14	49
S	343	0.52	50
AT	428	0.82	55
ZT	332	0.32	44

A quick inspection of the data in **Table 1** reveals that the NiW-x sulfided catalysts resulted highly selective to the DDS pathway regardless of the support. For example, the first step of 3MT transformation resulted in 99.7% by the DDS route for the NiW/A catalyst while for NiW/T and NiW/Z led around 98.5%. In the case of the NiW/AT and NiW/ZT the DDS decreased slightly to 97.6% and 95.8%, respectively. These findings confirm our previously reported results for the NiW system supported on binary Al_2O_3 - Ga_2O_3 mixed oxides [3]. Moreover, in all cases, the product yields indicated a significant production of isoprene near to 25% of the total DDS stream. Meanwhile, the C5-olefins production reached an average of 74% of the total DDS stream. It is important to mention that we observed only 1% of iso-paraffins production. These results exhibited suitable catalytic properties of the NiW systems for the highly selective HDS of fluid catalytic cracking naphtha. Additionally, we confirmed the order of stability for the C5-olefins reported by Dos Santos et al. [21]. The C5-olefins proportion resulted on average as follows: 91% of 2M2BT, 6% of 2M1BT and only 3% of 3M1BT.

3.2. Supports characterization

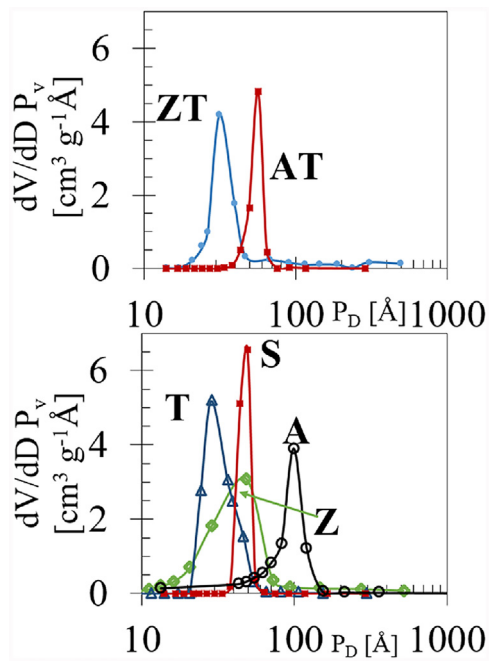
3.2.1. Textural properties

The textural properties of all calcined samples such as surface area, pore volume, and pore size distribution were obtained from the N_2 adsorption-desorption isotherms. Specific surface area, total pore volume and average pore size of the pure and mixed oxides are shown in **Table 2**. In this table it is appreciated that the specific surface areas include a broad range of values from 55 $\text{m}^2 \text{ g}^{-1}$ for T sample to 428 $\text{m}^2 \text{ g}^{-1}$ for AT sample. It was possible to differentiate between pure oxides, materials with a relatively small surface area (T and Z) and relatively high surface area (A and S). As seen, the combination of pure oxides by sol-gel synthesis provides relative high surface area mixed oxides (AT and ZT). Among all the materials, mixed oxides had the largest surface area. In particular, sample AT resulted with 428 $\text{m}^2 \text{ g}^{-1}$ which represent a 33% greater than A (320 $\text{m}^2 \text{ g}^{-1}$) sample and 9.5 times more than T sample. Meanwhile, ZT sample developed on average, six times more surface area than pure oxides. The N_2 adsorption-desorption isotherms for oxides are shown in **Fig. 2**. Adsorption isotherm type IV was displayed by all materials evidencing the production of mesoporous materials. Pore structure distinguished significant differences. In all cases, pore volumes and average pore diameter were lower than those obtained for sample A. All materials exhibited H1 hysteresis loops with an appreciable difference in the pore structure.

The pore size distribution plots are shown in **Fig. 3**. Except for A sample (98 Å), the average pore diameter resulted in around 40–55 Å. For samples T and Z, the pore size distributions were wider than those obtained for the A and S pure oxides. In contrast, with pure oxides, narrow pore size distribution was depicted by mixed materials that showed sharp peaks centered at 44 and 55 Å, ZT and AT, respectively. Nevertheless, pore diameters for all supports were suitable for the intended application.

3.2.2. X-ray diffraction

XRD patterns obtained from sample A displayed bands reflections at 37°, 46° and 66.8° (2θ degrees), which are related to the

**Fig. 3.** BJH pore width distribution of the prepared samples.

planes (111), (100) and (110) of γ - Al_2O_3 phase. In the case of the T sample, anatase and traces of rutile crystallographic phases were consistent with the calcination temperature. The pattern was fitted by Rietveld analysis considering both phases. Results showed 83.4% of anatase (JCPDS-01-084-1285) phase and 16.6% of rutile (JCPDS-01-072-1148) phase. Spectrum corresponding to Z material displayed mainly monoclinic (JCPDS-00-007-0343) phase (81.6%) and a few peaks from tetragonal (JCPDS-01-080-2156) phase (18.4%). It is well known that monoclinic phase is the most thermodynamically stable among them, usually up to 1100 °C. Thus, the tetragonal phase is metastable [22–24]. No diffraction bands were observed for S sample at a wide angle. However, small angle diffraction spectrum clearly exhibited a narrow band at ca. 1.3° and a little shoulder near to 2.1°. This result suggests that S material probably has an organized structure, presumably as a honeycomb core [25]. Indeed, the adsorption/desorption isotherms revealed a very narrow pore size distribution centered at 5 nm. Binary oxides displayed patterns of low crystallinity, showing only a broad weak peak from 20° to around 40° centered at 31° in both materials. This could be a result of some nanocrystals of anatase phase in the AT sample or the anatase-monoclinic phases in the ZT material. Nevertheless, the absence of intense bands corresponding to the anatase and rutile or monoclinic and tetragonal phases indicated almost amorphous materials. Several reports about mixed oxides have shown a lack of crystallinity when a correct wt.% from the oxides is achieved, and this phenomenon is related to the formation of the solid solution [26]. The XRD diffraction patterns and phases quantification obtained for all calcined samples are provided as Supplementary information A2.

The XRD patterns obtained for the NiW catalysts (oxide state) were similar to those obtained for the supports. The one exception was NiW/S, which presented three well-defined bands at 23.1°, 23.6° and 24.5° (2θ degrees) related to the WO_3 (results not showed here), regarding the crystallographic data sheet JCPDS 00-002-0308. This result suggests that the S support has a weak interaction with W atoms allowing the formation of large crystals easily detected by XRD. The absence of diffraction bands related to the WO_3 or NiO in the remaining patterns suggests a good disper-

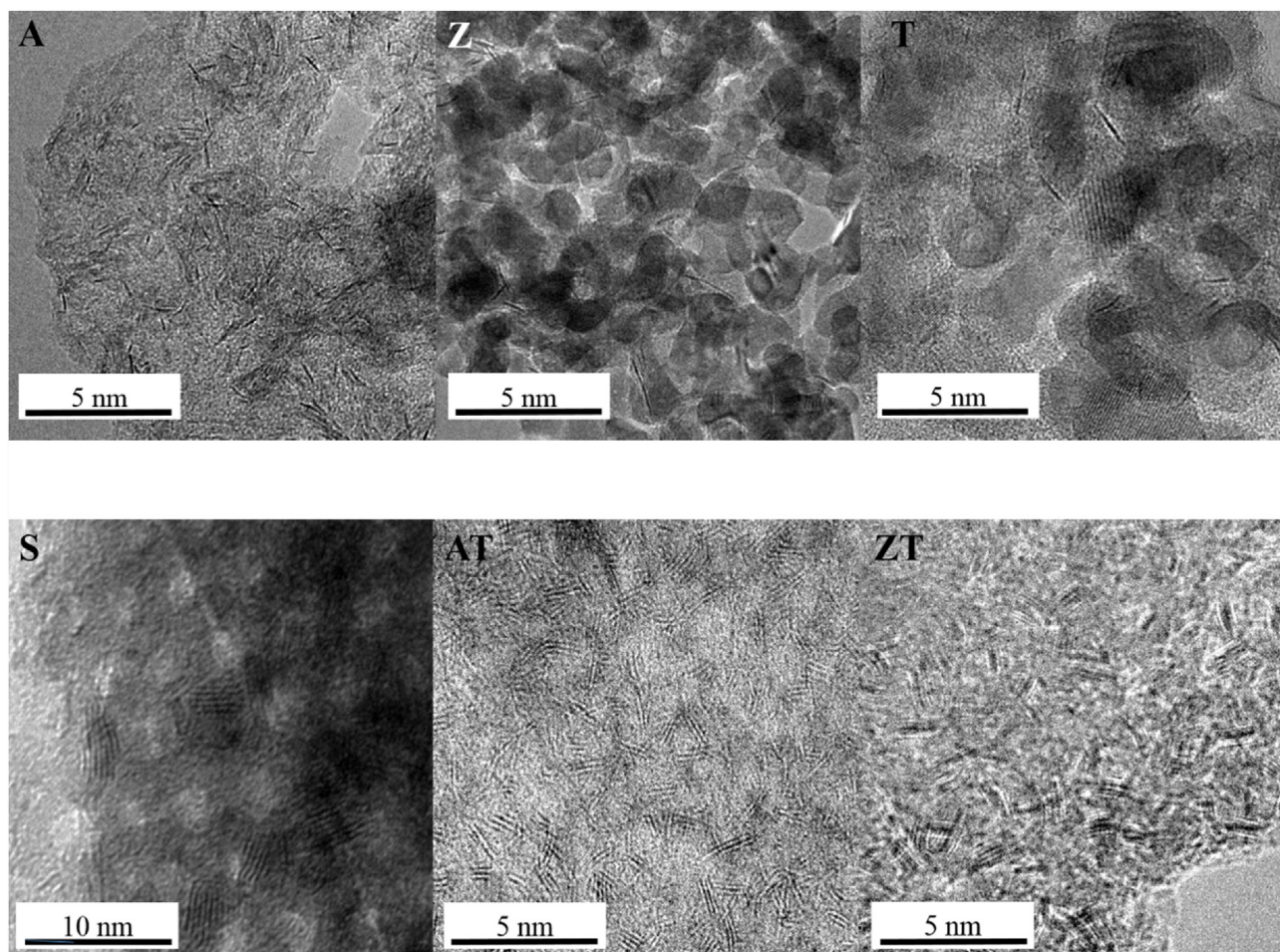


Fig. 4. HRTEM representative micrographs for NiW-x sulfided materials.

Table 3
Acidity of supports.

Sample	Normalized strength acid sites			
	weak%	medium%	strong%	^a total NH ₃ μmol g ⁻¹
	<200 °C	200–400 °C	>400 °C	
A	1.3	26.8	71.9	421
T	2.7	21.5	75.9	130
Z	0.4	18.0	81.7	183
S	0.9	37.2	61.9	361
ZT	3.0	33.0	64.0	245
AT	2.5	25.4	72.0	274

^a Calculated from the desorbed NH₃ by TPD profiles.

sion of the oxide precursors, at least below the detection limit of the technique.

3.2.3. Temperature-programmed desorption of NH₃

The acidity of the supports may induce improvements in the dispersion of the active metals and even an increase in activity, although a rapid deactivation of the acidic function was observed during the first hours of the reaction [27]. Usually, TPD of NH₃ adsorbed at low temperature provides three overlapped peaks [28]. Therefore, the region between 100 °C and 600 °C was fitted by Gaussian deconvolution, using three corresponding curves for different acidity strengths. These were assigned as follows: i) weak acidity (T < 200 °C), ii) medium acidity (200 °C < T < 400 °C) and iii) strong acidity (400 °C < T < 600 °C) as shown in Table 3. Results revealed

that A material exhibited the highest total acidity per gram of support (421 μmol NH₃/g) among all synthesized materials, only followed by siliceous oxide (361 μmol NH₃/g). Materials with a high percentage of strong acid sites resulted in samples Z (81.7%) and T (75.9%) and not those expected. AT (274 μmol NH₃/g) and ZT (245 μmol NH₃/g) mixed oxides resulted in very different behavior than the pure oxides. Both materials showed a total acidity higher than its respective pure oxides except for the pure alumina. The ZT sample displayed 23% more acidic sites than Z and 47% more than T materials. In the case of the AT mixed oxide, it has 35% less than A, and 52% more than T. Behavior observed for the mixed AT and ZT oxides was totally unexpected since both materials were synthesized by the same method and thermally treated at the same conditions than the pure materials. Also, it is possible to consider that the largest area in the mixed oxides could render in a higher quantity of acid sites than in the materials with the lower specific surface area. However, this fact was certainly not observed.

3.2.4. High-resolution transmission electron microscopy

Fig. 4 shows representative HRTEM images of the spent sulfided NiW/(x) catalysts. The presence of the typical black lines associated to the layered WS₂ nano-slabs was easily observed in all micrographs regardless of the support. As shown, the WS₂ slabs were homogeneously distributed and with different mean length and stacking degree, depending on the carrier. The micrograph related to the NiW/A sample (Fig. 4A) reveals that the WS₂ slabs resulted with low stacking degree, mainly formed by isolated individual layers suggesting strong interaction with the support [29].

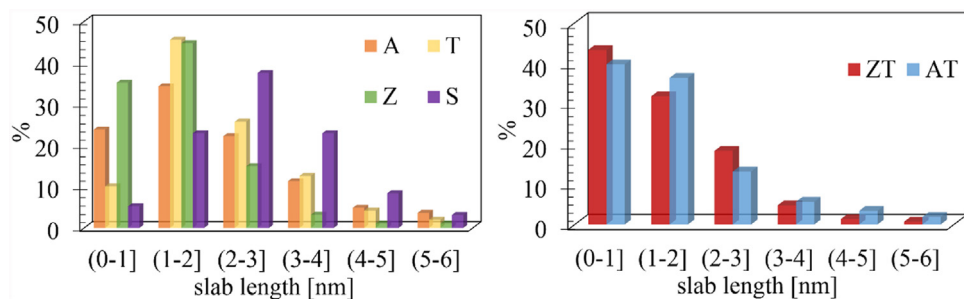


Fig. 5. Mean Length distribution for: (left) NiW/A, NiW/T, NiW/Z, NiW/S. (right) NiW/ZT, NiW/AT sulfided catalysts.

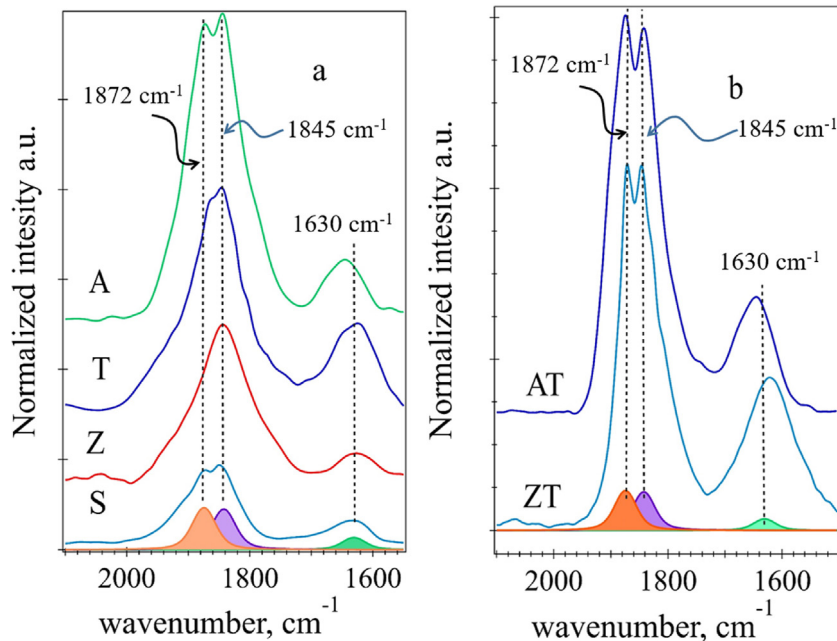


Fig. 6. FTIR spectra for the sulfided NiW/x series a) spectra for the NiW catalysts supported on pure oxides (A, T, S, and Z), b) spectra for the NiW catalysts supported on mixed oxides (AT and ZT).

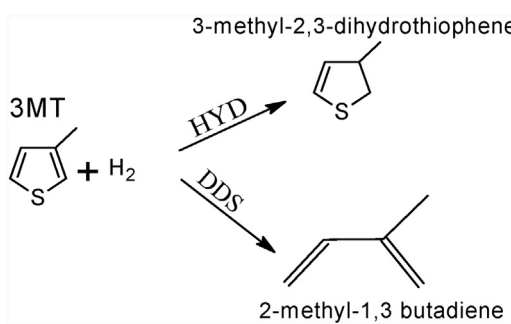
For a sample, NiW/Z (Fig. 4Z), the density of WS₂ nano-slabs clearly decreased, which is consistent with its W wt.% load. Interestingly, zirconia support displayed the formation of semi-spherical shaped nanoparticles with an average diameter of 1.3 ± 0.1 nm. The NiW/T (Fig. 4T) catalyst clearly displayed the planes related to the anatase phase and curve-shaped nano-particles, nearly similar to those observed in the zirconia sample. The active sulfide phase seems to be highly dispersed since we observed long isolated single layers. The micrograph for the NiW/S shows large groups of nano-slabs highly stacked, indicating that the active phase has a low dispersion degree. For the catalysts supported on the mixed oxides AT and ZT, the dispersion degree appears to be similar for both.

For each crystallite, two parameters have been considered: the average slab length (**L**) of the black lines and the stacking number (**N**) of three-dimensional stacked layers [29]. The compiled data are given in Table 4. There it can be seen that the **L** values obtained for the sulfided NiW/x catalysts are mainly distributed between 2 and 3 nm, except for the NiW/S which resulted with the highest **L** among series with 4.3 ± 0.3 nm. The **L** values increased as NiW/S > NiW/T > NiW/Z > NiW/A > NiW/ZT > NiW/AT. We observed that 80% of the slabs resulted between 1 and 3 nm for the NiW/A, NiW/Z, NiW/ZT and NiW/AT samples (see Fig. 5 left). Larger slabs (>3 nm) were nearly absent in the NiW/Z, NiW/ZT and NiW/AT catalysts (see Fig. 5 right). The observed average **N** values clearly show the effect of each support on the dispersion of the active phase. The

Table 4
HRTEM Statistical analysis for the sulfided NiW catalysts.

NiW-x	L	N
A	2.2	1.41
Z	2.5	1.25
T	2.9	1.24
S	4.3	4.40
ZT	2.1	2.54
AT	2.0	2.21

pure oxides exhibited the greater interaction with the W species among series, i.e. the fraction of single WS₂ slabs means about 63%, 78% and 81% for catalysts supported on A, T, and Z respectively. NiW/S sample considerably differs in comparison with the other catalysts; in this material, the average **N** resulted as high as 4.4 ± 0.3 layers, and this is in line with the poor dispersion suggested by the XRD pattern. For the catalysts supported on the AT and ZT mixed oxides, the average **N** data resulted in 2.2 ± 0.1 and 2.5 ± 0.2 layers respectively. Values slightly higher than in their respective catalysts supported on the single pure oxides (A, T or Z). It is clear that all these significant changes in the morphology are due to the metal-support interaction during the formation of the active NiWS phase. Therefore, as we observed, each support induces different slab length and stacking degree.



Scheme 1. Initial reaction step pathways of the transformation of 3MT.

3.2.5. FTIR of adsorbed NO on the sulfided catalysts

The surface of sulfided NiW catalysts was characterized by DRIFT measurements using NO as a probe molecule to identify the chemical state, nature and surface exposure of nickel and tungsten ions after catalyst sulfidation. The DRIFT spectra of NO absorption bands were normalized by the spot size and the total area of each sample. The normalized spectra of nitrogen monoxide adsorbed on the sulfided NiW/(x) catalysts are shown in Fig. 6. As seen, we observed two major bands around 1870 and at 1845 cm⁻¹ related to the NO adsorbed in the Ni²⁺ ions in oxidic and sulfided surroundings respectively [30,31]. A broadband located centered at 1630 cm⁻¹ was also obtained in all spectra. This band is usually associated with the isolated mono-nitrosyl species at the WS₂ edge or corner sites (W^{δ+}). As it can be expected, the intensities varied depending on the support due to the great differences in the Me-support interactions. The spectra obtained for the sulfided samples NiW/S, NiW/A, NiW/AT and NiW/ZT clearly displayed those three mentioned bands. However, the vibration related to the NO adsorbed in the Ni²⁺ oxide species at 1872 cm⁻¹ resulted with a low intensity in the spectra of NiW/T and NiW/Z samples. For the remaining sulfided samples, this band is almost of the same intensity than that associated to the NO adsorbed in the Ni²⁺ sulfided species, indicating a partial sulfidation of Ni promoter species upon the sulfidation conditions employed. Considering that the sulfided fraction of Ni is fully related to the so-called nonstoichiometric NiWS phase and therefore with the promotion, the analysis of the relative intensities and the ratio between NiS/NiOx species was obtained by Gaussian deconvolution. The used bands and positions are indicated in Fig. 6a and b as filled curves. The relative intensity for the species NiS resulted with the next trend: NiW/AT > NiW/ZT > NiW/A > NiW/T > NiW/Z > NiW/S. The ratio NiS/NiOx resulted higher than the unit for the catalysts supported in the pure oxides (NiW/A = 1.03, NiW/T = 1.45, NiW/Z = 1.40, NiW/S = 1.06) showing a better relative sulfidation over these samples. In the case of the catalysts supported on binary mixed oxides NiW/AT and NiW/ZT the ratio resulted in 0.97 and 1.00, respectively. For the asymmetric band around 1630 cm⁻¹ assigned to the W⁴⁺ ions surrounded by sulfur we observed

clear differences in the maximum position, probably related to W interaction with each support. Only the NiW sulfided catalysts supported in S, Z and T presented their maxima of this peak at 1630 cm⁻¹, although also their intensities presented notorious differences. The maxima of this peak for NiW/A and NiW/AT are shifted about 15 cm⁻¹ to higher frequencies (1645 cm⁻¹). While for the NiW/ZT the maximum shifted around 10 cm⁻¹ to a lower frequency (1620 cm⁻¹). The change to a higher wavenumber indicates that in these two samples the back donation of electrons from tungsten species to the bonding orbital of NO is greater, in comparison with the others samples. Contrary to these observations, the shift to a lower frequency observed in the NiW/ZT sample indicates a lower electron back donation from tungsten species to the bonding orbital of NO. In conclusion, these shifts observed could be attributed to the interaction of the Ni species with W [32]. Finally, no evidence of the formation of di-nitrosyl species related to NO adsorbed at the S-edge was observed in any spectra around 1817–1687 cm⁻¹.

4. Discussion

4.1. Reaction pathways

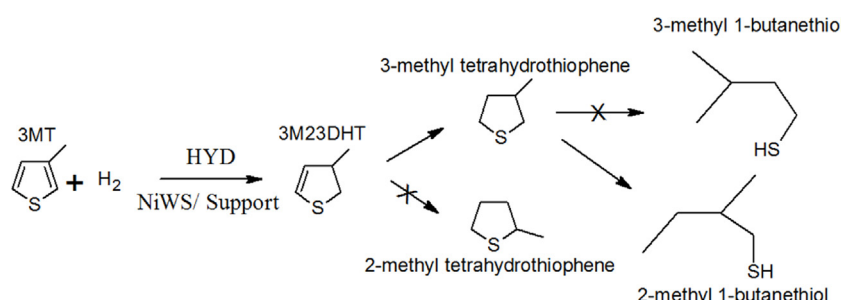
The 3MT transformation may be occurring along two possible routes (Scheme 1): the direct desulfurization (DDS) and the hydrogenation (HYD) [3]. After this initial step, it is possible to observe several products in the stream. Therefore, we carefully analyzed the experimental reaction products to establish a scheme with all observed reaction steps for the 3MT HDS reaction. Our results revealed that during the first HYD step it is saturated one of the double bonds of the ring to produce 3-methyl-2,3-dihydrothiophene (3M2,3DHT) and for the DDS, the first product would be 2-methyl-1,3-butadiene (isoprene).

In the second hydrogenation path, the 3-methyl tetrahydrothiophene (3MTHT) or 2-methyl tetrahydrothiophene may be produced, although the latter is a product of an isomerization reaction, and it was not experimentally detected. Later, the 3MTHT could present a ring opening reaction to produce 3-methyl 1-butanethiol (3M1BT) or 2-methyl 1-butanethiol (2M1BT), but again, only traces of 2M1BT were detected (Scheme 2). Thus, isomerization was ruled out for our catalysts.

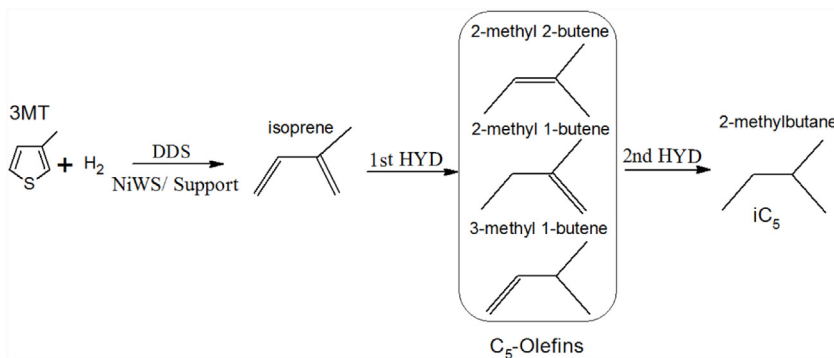
Throughout the DDS route, isoprene may be hydrogenated to produce C₅-olefins: 2-methyl-2-butene (2M2BN), 2-methyl-1-butene (2M1BN) and 3-methyl-1-butene (3M1BN). Finally, after a second hydrogenation, the C₅-olefins may transform into 2-methyl-butane (iC₅) as shown in the Scheme 3. It is worth mentioning that we observed all possible products of the DDS pathway in the out-stream reactor.

4.2. Support effects

As it was mentioned, the fluid catalytic cracking naphtha is the main component of commercial gasoline. Therefore, it is of



Scheme 2. Full scheme of the 3MT hydrogenation pathway.



Scheme 3. Full scheme of the 3MT direct desulfurization pathway.

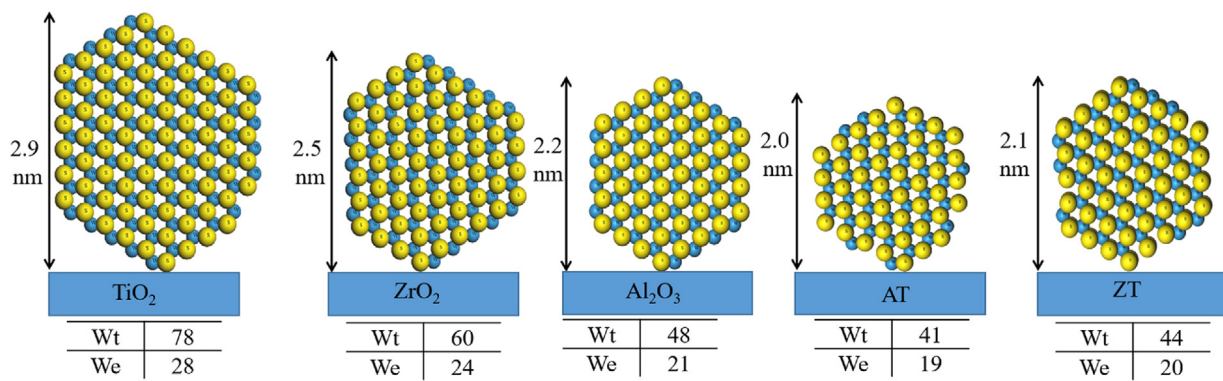


Fig. 7. Schematic representation of the average slab length and morphology data for the WS₂ sulfide phase over the different supports. Blue: tungsten, Yellow: sulfur.

paramount importance to selectively remove sulfur from this pool. However, as the FCC gasoline contributes with around of 90% of the total sulfur in this stream and is composed by aromatics, olefins, and iso-olefins that help to meet the high octane number requirements [3]. Therefore, high activity in HDS and mild hydrogenation properties are desirable to avoid excessive olefins saturation. The catalytic activity results showed in these terms that the catalysts with the highest activity among the series were NiW/AT and NiW/ZT. A careful examination of the selectivity results pointed out to NiW/A and NiW/AT as the catalysts with the lesser olefin saturation properties among the studied materials. The first one because the initial step of the reaction was mainly the DDS pathway and the second one because it showed the highest production of isoprene among all catalysts (See Table 1). For supported NiW sulfided catalysts a gain of activity is well explained by an increase in the dispersion of the active WS₂ phase, by a better sulfidation and a higher number of promoted sites [29]. As we observed by HRTEM, each support led to different characteristics of the WS₂ phase. With the WS₂ average slab length, we are able to calculate the average atoms which are forming each slab. Hence, following Kastelan geometric model [33], the methodology proposed by Vrinat et al. [34], the average slab length and the bond distance between W to W (d_{W-W}) from the EXAFS study [35] the calculation of the slab parameters was done. We present in Fig. 7 the obtained results for the total number of W atoms (W_t) forming each slab and the presumed to be catalytically active W atoms in the edge of the slab (W_e).

The data obtained for the NiW/S resulted in $W_t = 160$ atoms and $W_e = 41$ atoms; these values are out of the scale to those presented in Fig. 7, consequently are not included there. We observed an increase of W atoms in the edge with the growth in the slab length. This phenomenon could induce a lesser promotion of the WS₂ active phase and therefore the observed variation in the catalytic activity. Recent studies have revealed that a better promotion of the

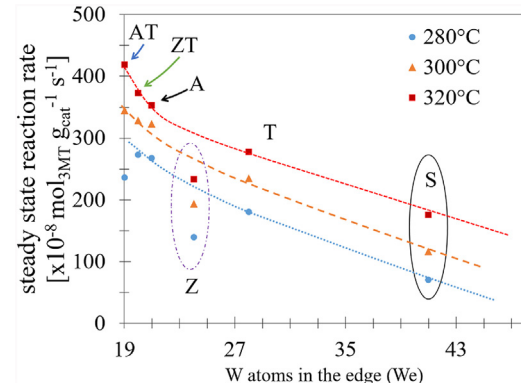


Fig. 8. Steady state catalytic activity as a function of the number of W_e .

WS₂ slabs render a higher activity and could modify the selectivity [36–38]. In this case, all materials were prepared with the same Ni/(Ni + W) promotion ratio, but the interaction with each support derived into a different morphology of the active phase. This also could induce a modification in the selectivity as we observed. For example, in the steady state hydrogenation reaction rate at 280 °C for the sulfided NiW/ZT (11.5 mol_{3MT} g_{cat}⁻¹ s⁻¹) the hydrogenation pathway resulted in almost two and 14 times fold than for the NiW/AT (5.66 mol_{3MT} g_{cat}⁻¹ s⁻¹) or NiW/A (0.81 mol_{3MT} g_{cat}⁻¹ s⁻¹) respectively. Besides, as we expected, the trend in catalytic activity correlates well with the catalytically active W atoms in the edge (W_e) of the slab in all the range of temperatures tested. Fig. 8 displays the correlation between the catalytic activity for the sulfided NiW series and the number of W_e atoms.

Early studies of Topsøe et al. [39] using in situ FT-IR spectroscopy combined with NO adsorption were carried out to examine the

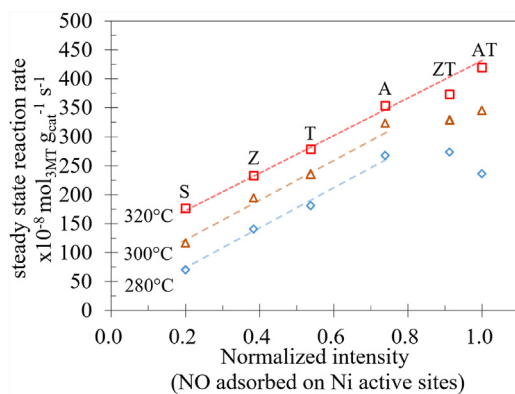


Fig. 9. Steady state catalytic activity as a function of the normalized intensities of NO adsorbed on Ni^{2+} sites.

adsorption on sulfided Co-Mo/Al₂O₃ catalysts. They found that thiophene HDS activity of the CoMo/Al₂O₃ catalyst correlated well with IR band intensity of NO adsorbed on the Co sites. Based on these results, they proposed that the addition of Co-lead to the formation of the so-called Co-Mo-S phase, in which Co atoms hinder Mo atoms located at the edge site of the MoS₂ slab. Therefore, similarly in our sulfided NiW catalysts, information provided by this probe allows us to determine the NO adsorption on sites susceptible to act as active sites on the surface of the catalyst. Then, assuming that NO adsorption sites correspond to Ni active sites, the normalized intensities of the vibrational mode of NO at 1845 cm⁻¹ were obtained. Then the catalytic activity was plotted as a function of the normalized intensity as it is shown in Fig. 9.

As it is possible to observe the intrinsic catalytic activity on the HDS of 3MT correlates well with the normalized intensities data of NO adsorbed on Ni active sites obtained in all the range of temperatures tested, but particularly in the higher one (320 °C). Similar linear correlations have been reported for NiW base catalysts in reactions carried out at elevated temperatures (>300 °C) with the NO adsorbed on Ni²⁺ sulfur sites for example, thiophene (350 °C) and 4,6-Dimethyl-Dibenzothiophene (4,6DMDBT) (340 °C) HDS [31,32], naphthalene (300 °C) HYD [40], pyridine hydrodenitrogenation (HDN) (350 °C) [32] among others model reactions. In the NiW catalyst supported on the pure oxides S, Z, T, and A, the trend is entirely linear in all range of temperatures. Catalysts supported on the mixed oxides seems to fall out the trend partially, particularly at the lowest reaction temperature (280 °C). Likewise, it is important to highlight that the NiW/ZT catalysts resulted with a better activity in comparison with the catalysts prepared over the pure oxides Z and T.

The use of this probe permitted us to confirm that the intensity related to the NO adsorption on the W^{δ+} sulfided species do not correlate with the activity as several authors have suggested [41]. Furthermore, if the NO adsorption is related to the edge sites of the WS₂ slabs, the adsorbed amount of NO should be proportional to the metal available in each material [41,42]. Nevertheless, it is not the tendency observed; as we showed in previous paragraphs, the slab length increased, and the intensity of the frequency at 1630 cm⁻¹ decreased. Even when the trend is not linear, particularly in the NiW/T sulfided sample, such assumption seems to be confirmed by the observed experimental results. Besides, as we mentioned before, the catalytic activity in HDS reaction is attributed to the non-stoichiometric Ni-W-S phase. However, this phase is formed when the edge or corners sites of the WS₂ slabs are decorated by Ni species, then the promotion effect occurs. In simplistic terms, the WS₂ slabs are also functioning as a support for the Ni species. Consequently, the quantity of NO adsorbed on the W sulfur edges decreases depending on the Ni relative promotion to the active

phase. Hence, as higher the promotion is, meaning the formation of the NiWS active phase, the adsorption of NO over the W⁴⁺ species should decrease. Considering the former, it is evident why the NO adsorbed on Ni²⁺ sulfide species correlate well with the activity and not with the NO adsorbed on the W⁴⁺ sulfide species.

For supported catalysts, the primary role of the support is to improve the dispersion of the active phases and in many cases avoid the sintering under catalytic reaction conditions. Moreover, it is important to highlight the paramount role of the catalysts preparation. Parameters as the pH, the metal concentration of an impregnating solution and the isoelectric point (IEP) have an impact on the structure of the supported metal oxides [43]. Likewise, the catalyst supports frequently have an influence on the catalytic properties of the supported metals through electronic or structural interactions [44]. Recently many groups have reported the preparation of NiW based catalysts studying parameters such as the IEP [29,43,45] the impregnation pH [45,46] or the use of quelant agents [31,46,47]. However, even by using alumina with different crystalline structures to prepare the NiW catalysts, the formation of the NiWS phase present clear differences [16]. Our group has reported that the interaction of the support with the metallic poli-oxo species in the aqueous solution could have an impact on the size of the W [43] and Ni clusters [29]. In that direction, it is worth to mention that the IEP of the materials plays a paramount role in the preparation of the samples. In this case, all materials have an intrinsic IEP very different between each other with values from 3.0 for SiO₂, 5.1 for titania, 7.1 for ZrO₂ to 9.0 for alumina [48]. Thus impregnate with solutions at pH up to the IEP must be avoided particularly when the impregnation solutions with ammonium metatungstate have an experimental pH around 3.7, and only the anionic HW₆O₂₁⁵⁻ species are present as in our case [29]. Therefore, in our study, the electrostatic interaction of the poli-oxotungstates in the impregnation solution with the supports during the synthesis procedure was accurate for all samples except for the siliceous materials. This seems to be the genesis of the lower catalytic properties observed for the NiW/S catalysts among series. Further work by other techniques such as UV-vis, FTIR of adsorbed pyridine, XPS on the sulfided materials and density functional theory calculations are in progress to help to understand the metal-support interaction on these series.

5. Conclusions

The NiW catalysts demonstrated clear differences in their morphology of the active sulfur phase regarding each support. We observed an increase of W atoms in the edge with the growth in the slab length. This phenomenon could induce a lesser promotion of the WS₂ active phase and therefore the observed variation in the catalytic activity. The outstanding performance of the NiW/AT and NiW/ZT catalysts may be attributed to modulation of the support active phases interaction due to the mix of supports. The combination of the observed slab length and the stacking degree parameters ($L \approx 2.05 \pm 0.05$, $N \approx 2.37 \pm 0.16$) for these materials seems to be the optimal values to obtain the enhanced catalytic activity. The promotion of the active phase, therefore, is higher when the optimal slab and stacking parameters are reached. As it was observed, the intrinsic catalytic activity on the HDS of 3MT correlates well with the normalized intensities data of NO adsorbed on Ni active sites. The high surface area displayed by A, AT, ZT and the S material do not impact the dispersion of the WS₂ nano-slabs, rather this is attributed to the intrinsic properties of each support as the acidity observed by NH₃ adsorption or the point of zero charge. By these results exhibited, we postulate that the mixed supports induced higher catalytic performance on the 3MT HDS reaction. Therefore, it can be the way to modulate the metal-support inter-

action. Finally, this study has shown suitable catalytic properties of the NiW system for the highly selective HDS of fluid catalytic cracking naphthas.

Acknowledgements

The authors are grateful to F. Ruiz and E. Aparicio for its expert technical assistance and to the project SENER-CONACyT 117373 for the financial support. V.A. Suárez-Torillo, L.A. Zavala-Sánchez express their gratitude to CONACyT for their graduate fellowships.

Appendix A. Supplementary data

Supplementary data associated with this article can be found, in the online version, at <http://dx.doi.org/10.1016/j.apcatb.2017.05.014>.

References

- [1] A. Stanislaus, A. Marafi, M.S. Rana, *Catal. Today* 153 (2010) 1–68.
- [2] S. Shan, P. Yuan, W. Han, G. Shi, X. Bao, *J. Catal.* 330 (2015) 288–301.
- [3] J.N. Díaz de León, *Appl. Catal. B: Environ.* 181 (2016) 524–533.
- [4] J.A. Mendoza-Nieto, F. Robles-Méndez, T.E. Klimova, *Catal. Today* 250 (2015) 47–59.
- [5] Y. Okamoto, T. Kubota, *Catal. Today* 86 (2003) 31–43.
- [6] O.Y. Gutierrez, S. Singh, E. Schachtl, J. Kim, E. Kondratieva, J. Hein, J.A. Lercher, *ACS Catal.* 4 (2014) 1487–1499.
- [7] M. Breysse, C. Geantet, P. Afanasyev, J. Blanchard, M. Vrinat, *Catal. Today* 130 (2008) 3–13.
- [8] J. Arturo Mendoza-Nieto, Ivan Puente-Lee, Cecilia Salcedo-Luna, Tatiana Klimova, *Fuel* 100 (2012) 100–109.
- [9] C. Roukoss, D. Laurenti, E. Devers, K. Marchand, L. Massin, M. Vrinat, C.R. Chim. 12 (2009) 683–691.
- [10] L. Haandel, M. Bremmer, P.J. Kooyman, J.A. Rob van Veen, T. Weber, E.J.M. Hensen, *ACS Catal.* 5 (2015) 7276–7287.
- [11] R.M. Casagrande, W.K. Meerbott, A.F. Sartor, R.P. Trainer, *Ind. Eng. Chem.* 47 (4) (1955) 744.
- [12] S. Brunet, D. Mey, G. Perot, C. Bouchy, F. Diehl, *Appl. Catal. A: Gen.* 278 (2005) 143–172.
- [13] I.R. Galindo, J.A. de los Reyes, *Fuel Process. Technol.* 88 (2007) 859–863.
- [14] M.C. Barrera, M. Viniegra, J. Escobar, M. Vrinat, F. de los Reyes, J. García, *Catal. Today* 98 (2004) 131–139.
- [15] T.K.T. Ninh, L. Massin, D. Laurenti, M. Vrinat, *Appl. Catal. A: Gen.* 407 (2011) 29–39.
- [16] D. Laurenti, B. Phung-Ngoc, C. Roukoss, E. Devers, K. Marchand, L. Massin, L. Lemaitre, C. Legens, A.A. Quoineaud, M. Vrinat, *J. Catal.* 297 (2013) 165–175.
- [17] M.J. Vissenberg, Y. van der Meer, E.J.M. Hensen, R.A. van Santen, V.H.J. de Beer, A.M. van der Kraan, J.A.R. van Veen, *J. Catal.* 198 (2001) 151–163.
- [18] T.A. Zepeda, A. Infantes-Molina, J.N. Díaz de León, S. Fuentes, G. Alonso-Núñez, G. Torres-Otañez, B. Pawelec, *Appl. Catal. A: Gen.* 484 (2014) 108–121.
- [19] J.A. Mendoza-Nieto, O. Vera-Vallejo, L. Escobar-Alarcón, D. Solís-Casados, T. Klimova, *Fuel* 110 (2013) 268–277.
- [20] Y. Li, D. Pan, C. Yu, Y. Fan, X. Bao, *J. Catal.* 286 (2012) 124–136.
- [21] N. Dos Santos, H. Dulot, N. Marchal, M. Vrinat, *Appl. Catal. A: Gen.* 352 (2009) 114–123.
- [22] M. Yashima, M. Kakihana, M. Yoshimura, *Solid State Ionics* 86–88 (1996) 1131–1149.
- [23] A. Trovarelli, *Catalysis by ceria and related materials Catalytic Science Series*, vol. 2, Imperial College Press, 2002, pp. 15–17, 217–224.
- [24] L. Kokporka, S. Onsuratoom, T. Puangpetch, S. Chavadej, *Mater. Sci. Semicond. Process.* 16 (2013) 667–678.
- [25] H. Song, J. Wang, Z. Wang, H. Song, F. Li, Z. Jin, *J. Catal.* 311 (2014) 257–265.
- [26] H. Zou, Y.S. Lin, *Appl. Catal. A: Gen.* 265 (2004) 35–42.
- [27] M. Breysse, P. Afanasyev, C. Geantet, M. Vrinat, *Catal. Today* 86 (2003) 5–16.
- [28] B. Hunger, J. Hoffmann, O. Heitzsch, M. Hunger, *J. Therm. Anal.* 36 (1990) 1379.
- [29] J.N. Díaz de León, M. Picquart, L. Massin, M. Vrinat, J.A. de los Reyes, *J. Mol. Catal. A: Chem.* 363–364 (2012) 311–321.
- [30] A. Benítez, J. Ramírez, J.L.G. Fierro, A. López Agudo, *Appl. Catal. A: Gen.* 144 (1996) 343–364.
- [31] Y. Fan, H. Xiao, G. Shi, H. Liu, Y. Qian, T. Wang, G. Gong, X. Bao, *J. Catal.* 279 (2011) 27–35.
- [32] A. Benítez, J. Ramírez, J.L.G. Fierro, A. Lopez Agudo, *Appl. Catal. A: Gen.* 144 (1996) 343–364.
- [33] S. Kasztelan, H. Toulhoat, J. Grimblot, J.P. Bonnelle, *Appl. Catal.* 13 (1984) 127–159.
- [34] M. Vrinat, M. Breysse, C. Geantet, J. Ramírez, F. Massoth, *Catal. Lett.* 26 (1994).
- [35] S.D. Kelly, N. Yanga, G.E. Mickelson, N. Greenlay, E. Karapetrova, W. Sinkler, S.R. Bare, *J. Catal.* 263 (2009) 16–33.
- [36] C.E. Santolalla-Vargas, V.A. Suárez Torillo, J.A. de los Reyes, D.K. Cromwell, B. Pawelec, J.L.G. Fierro, *Mater. Chem. Phys.* 166 (2015) 105–115.
- [37] T. Alphazan, A. Bonduelle-Skrzypczak, C. Legens, Z. Boudene, A.L. Taleb, A.S. Gay, O. Ersen, C. Copréret, P. Raybaud, *J. Catal.* 340 (2016) 60–65.
- [38] Luis G. Woolfolk, C. Geantet, L. Massin, D. Laurenti, J.A. De los Reyes, *Appl. Catal. B: Environ.* 201 (2017) 331–338.
- [39] N.Y. Topsøe, H. Topsøe, *J. Catal.* 84 (1983) 386.
- [40] T. Halachev, P. Atanasova, A. Lopez Agudo, M.G. Arias, J. Ramírez, *Appl. Catal. A: Gen.* 136 (1996) 161–175.
- [41] T.A. Zepeda, B. Pawelec, J.N. Díaz de León, J.A. de los Reyes, A. Olivas, *Appl. Catal. B: Environ.* 111–112 (2012) 10–19.
- [42] X. Wang, U.S. Ozkan, *J. Catal.* 227 (2004) 492–501.
- [43] J.N. Díaz de León, M. Picquart, M. Villarroel, M. Vrinat, F.J. Gil Llambias, J.A. de los Reyes, *J. Mol. Catal. Chem.* A 323 (2010) 1–6.
- [44] M. Pérez De la Rosa, M.J. Yácaman, S. Texier, A. Mehta, F. Murrieta, G. Berhault, S. Fuentes, A. Camacho, J.A. Montoya, R.R. Chianelli, *J. Catal.* 225 (2004) 288–299.
- [45] A.E. Cruz-Perez, A. Guevara-Lara, J.P. Morales-Ceron, A. Alvarez-Hernandez, J.A. de los Reyes, L. Massin, C. Geantet, M. Vrinat, *Catal. Today* 172 (2011) 203–208.
- [46] V.A. Suárez-Torillo, C.E. Santolalla-Vargas, J.A. de los Reyes, A. Vázquez-Zavala, M. Vrinat, C. Geantet, *J. Mol. Catal. A: Chem.* 404–405 (2015) 36–46.
- [47] H. Li, M. Li, Y. Chu, F. Liu, H. Nie, *Appl. Catal. A: Gen.* 403 (2011) 75–82.
- [48] M. Kosmulski, *Adv. Colloid Interface Sci.* 152 (2009) 14–25.